6044 *Chem. Mater.* **2010,** *22,* 6044–6055
DOI:10.1021/cm100469y

CHEMISTRY OF MATERIALS
Article

Anisotropic Crystal Growth Kinetics of Anatase TiO_2 Nanoparticles Synthesized in a Nonaqueous Medium

Grethe Vestergaard Jensen,[†] Martin Bremholm,[†] Nina Lock,[†] G. Roshan Deen,[†] Torben R. Jensen,[†] Bo B. Iversen,[†] Markus Niederberger,[‡] Jan Skov Pedersen,[†] and Henrik Birkedal*[,†]

[†]*Department of Chemistry & Interdisciplinary Nanoscience Center (iNANO), University of Aarhus, Langelandsgade, DK-8000 Aarhus, Denmark, and* [‡]*Department of Materials, ETH Zürich, Wolfgang-Pauli-Strasse 10, 8093 Zürich, Switzerland*

Received February 14, 2010. Revised Manuscript Received September 23, 2010

The formation and growth of titania (anatase) nanoparticles in benzyl alcohol from $TiCl_4$ was studied in situ at 85 °C via powder X-ray diffraction (PXRD), small-angle X-ray scattering (SAXS), and turbidimetry. The results provide new information on the kinetics of this process and allow for better control of particle size, shape, and aggregation. Rietveld refinement of ex situ PXRD data shows that the final crystals are anisotropic in shape and elongated along the crystallographic *c*-axis. In situ SAXS and PXRD show that the crystals form suddenly after a lag period. The crystals are initially isotropic in shape and the growth is isotropic; thereafter, the growth proceeds predominantly along the crystallographic *c*-axis to form anisotropic crystals, in agreement with the ex situ PXRD results. The relative lattice strain, which is determined as the lattice deformation relative to the lattice constants found late in the growth process, is positive along the *c*-axis and negative, but smaller, along the *a*-axis. In both directions, the strain relaxes as the particles grow. The strain anisotropy, measured as c/a, relaxes to the bulk value for particles with an equivalent linear dimension on the order of 4.5 nm. The present data provide the first strain information in anisotropic particles smaller than ~5 nm. The large anisotropic strain is related to the important out-of-plane contributions to the surface energy resulting from selective ligand binding to the surfaces. In situ SAXS shows that the particles initially form small aggregates that can be modeled as either spheres or surface fractals. The aggregate radius of gyration shows a linear growth for both models. At long growth times, the turbidity suddenly increases, because of the occurrence of large-scale aggregation. The onset time follows Arrhenius behavior with an effective activation energy of 106.7 kJ/mol. The large scale aggregation is also reflected in the in situ SAXS data as the point after which the aggregate size accelerates and the aggregates can only be described as volume fractals. These types of sol−gel syntheses are typically stopped after the large-scale aggregation; however, according to the present work, discrete or only slightly aggregated nanoparticles are present at a much earlier stage.

Introduction

Understanding the kinetics of nanoparticle formation is the key to controlling the properties of the synthesis products.[1] Metal oxide nanoparticles have a wealth of uses.[1] Of special interest is crystalline titania, since it has a wide range of applications, including catalysis,[2,3] gas sensing,[4] photovoltaics,[5,6] and pigmentation and reflective coatings.[7] For all of these applications, crystal properties such as polymorphs, size, and shape are crucial to the performance. Thus, understanding and hence controlling the titania synthesis is of great importance. Significant insights into growth kinetics can be obtained from ex situ studies,[8,9] but they are limited in several aspects, including the fact that sampling only occurs at distinct times and the fact that the obtainable time resolution is limited. The use of in situ structural characterization techniques[10] on these systems is not trivial, but significant advances have been made, e.g., using high- and medium-energy synchrotron radiation[11−15] or neutrons.[16]

*Author to whom correspondence should be addressed. Tel.: +45 89423887. Fax: +45 86196199. E-mail: hbirkedal@chem.au.dk.

(1) Fernández-García, M.; Martínez-Arias, A.; Hanson, J. C.; Rodriguez, J. S. *Chem. Rev.* **2004**, *104*, 4063.
(2) Zhang, Z.; Wang, C.-C.; Zakaria, R.; Ying, J. Y. *J. Phys. Chem. B* **1998**, *102*, 10871.
(3) Andersson, M.; Birkedal, H.; Franklin, N. R.; Ostomel, T.; Boettcher, S.; Palmqvist, A. E. C.; Stucky, G. D. *Chem. Mater.* **2005**, *17*, 1409.
(4) Ferroni, M.; Carotta, M. C.; Guidi, V.; Martinelli, G.; Ronconi, F.; Sacerdoti, M.; Traversa, E. *Sens. Actuators B* **2001**, *77*, 163.
(5) Hagfeldt, A.; Grätzel, M. *Acc. Chem. Res.* **2000**, *33*, 269.
(6) McFarland, E. W.; Tang, J. *Nature* **2003**, *421*, 616.
(7) Langlet, M.; Burgos, M.; Coutier, C.; Jimenez, C.; Morant, C.; Manso, M. *J. Sol−Gel Sci. Technol.* **2001**, *22*, 139.
(8) Oskam, G.; Nellore, A.; Penn, R. L.; Searson, P. C. *J. Phys. Chem. B* **2003**, *107*, 1734.
(9) Finnegan, M. P.; Zhang, H.; Banfield, J. F. *Chem. Mater.* **2008**, *20*, 3443.
(10) Dey, A.; de With, G.; Sommerdijk, N. A. J. M. *Chem. Soc. Rev.* **2010**, *39*, 397.
(11) Jensen, H.; Bremholm, M.; Nielsen, R. P.; Joensen, K. D.; Pedersen, J. S.; Birkedal, H.; Chen, Y.-S.; Almer, J.; Søgaard, E. G.; Iversen, S. B.; Iversen, B. B. *Angew. Chem., Int. Ed.* **2007**, *46*, 1113.

Published on Web 10/21/2010

This study addresses the nonaqueous sol−gel synthesis of nanocrystalline TiO_2 (anatase) proposed by one of us.[17,18] It gives particles 3−7 nm in size, depending on the synthesis conditions. Titanium tetrachloride is added to benzyl alcohol, which acts both as a solvent and an oxygen supplier in the sol−gel reaction. Benzyl groups are attached to the final particles and help to stabilize their small size. Here, we show that the nanocrystals obtained are anisotropic in shape and investigate the mechanism of their formation. By combining complementary techniques and using these to study the reaction in situ, one can follow the reaction on length scales from the atomic scale to the mesoscopic scale. The methods used in the present paper are synchrotron powder X-ray diffraction (PXRD), small-angle X-ray scattering (SAXS), and turbidimetry. PXRD samples the crystalline phase of the particles and the crystal size for nanosized crystals by diffraction peak broadening. SAXS provides information of particle shape and size on length scales from 1 nm to 100 nm. The turbidity samples the concentration of particles whose size is on the order of the applied wavelength and is thus particularly sensitive to particle aggregation. It is found that crystalline spherical particles form first, subsequently grow into anisotropic shapes, and then aggregate. The onset of growth anisotropy is related to the observation of large anisotropic lattice strain.

Experimental Section

Synthesis. The synthesis followed the published procedure of Niederberger et al.,[18,19] with the modification that $TiCl_4$ was presolvatized in absolute ethanol prior to addition to the reaction solvent.[19] This was done to obtain a less-violent reaction. In a typical procedure, 1.73 g (equal to 1 mL) $TiCl_4$ was added to 5 mL of 99.9% ethanol while stirring. This gave a yellow solution, which was added to 34.6 g of benzyl alcohol ($C_6H_5CH_2OH$), giving a $TiCl_4$-to-benzyl alcohol weight ratio of 1:20. The same reactant ratio was applied in all syntheses.

For the synthesis of product for ex situ analyses, the reaction mixture was heated to the desired temperature in an oil bath and kept there under stirring until a heavy white precipitate was present. Thereafter, the reaction was stopped (cooled to room temperature). The precipitate was washed in ethanol and/or THF and dried in air at room temperature. Syntheses were performed at 40, 60, 80, 100, 120, and 150 °C. Some washed and dried synthesis products were redispersed in ethanol and investigated by TEM. The results were in general agreement with the results reported by Kotsokechagia et al.[19] and will not be discussed further.

To estimate the yield of the reaction, all solid material was collected via centrifugation after 472 min, which was the same reaction time used in the in situ SAXS experiment, in a reaction made separately from the SAXS measurements. This material was air-dried and weighed. This indicated an apparent yield of 150.3%. However, this includes surface-bound solvent. To obtain a measure of the true TiO_2 yield, the powder was subjected to thermogravimetric analysis/differential scanning calorimetry (TGA/DSC) analysis from 24 °C to 1200 °C, using a Netzsch Model STA 449 C system (Netzsch−Gerätebau GmbH, Selb, Germany), using Al_2O_3 crucibles and an atmosphere of helium with O_2 added to the purge gas. This resulted in a mass loss of 40.8 wt % (see Figure S1 in the Supporting Information). The residual mass indicated a yield of 89.0%. XRD data, collected on a STOE IPDS system, confirmed that the particles were nanocrystalline prior to analysis and that they transformed to rutile and sintered to macrocrystalline material during the heating process (see Figure S2 in the Supporting Information). We also attempted to use density measurements to derive the yield, but the limited precision with which it was possible to perform the measurements and the approximations involved rendered this approach intractable.

Ex Situ Powder X-ray Diffraction. Ex situ powder X-ray diffraction (PXRD) measurements for Rietveld refinement were performed for samples synthesized at different temperatures on a Bruker Model D8 powder diffractometer using Cu $K\alpha_1$ (λ = 1.54056 Å) radiation that had been further collimated by Soller slits for improved angular resolution. The diffraction patterns were refined by the Rietveld method using the program FULLPROF.[20,21] Anisotropic size peak broadening clearly was needed to fit the diffraction pattern. This was included using a spherical harmonic expansion of the crystal shape, as implemented in the program. For all refinements, anisotropic atomic displacement parameters were fixed at values taken from the literature,[22] since refinement of these parameters led to unphysical values. The instrumental resolution function was determined using a Si standard (NIST SRM640) and was taken into account in the fitting procedure.

Synchrotron In Situ PXRD. In situ PXRD measurements were performed using a home-built furnace that was based on a stream of hot air. The liquid sample was placed in a 1-mm borosilicate capillary. The measurements were made at the Beamline ID7-11 facility at the MAXII synchrotron in Lund, Sweden, using 1.1072 Å X-rays, a beam diameter of 0.5 mm, and a MAR 165 CCD detector.[23] The exposure time was 30.0 s, which, combined with the

(12) Norby, P. *Curr. Opin. Colloid Interface Sci.* **2006**, *11*, 118.
(13) Michailovski, A.; Grunwaldt, J.-D.; Baiker, A.; Kiebach, R.; Bensch, W.; Patzke, G. R. *Angew. Chem., Int. Ed.* **2005**, *44*, 5643.
(14) Li, J.; Cookson, D. J.; Gerson, A. R. *Cryst. Growth Des.* **2008**, *8*, 1730.
(15) Abécassis, B.; Testard, F.; Spalla, O.; Barboux, P. *Nano Lett.* **2007**, *7*, 1723.
(16) Walton, R. I.; Millange, F.; Smith, R. I.; Hansen, T. C.; O'Hare, D. *J. Am. Chem. Soc.* **2001**, *123*, 12547.
(17) Niederberger, M.; Bartl, M. H.; Stucky, G. D. *J. Am. Chem. Soc.* **2002**, *124*, 13642.
(18) Niederberger, M.; Bartl, M. H.; Stucky, G. D. *Chem. Mater.* **2002**, *14*, 4364.
(19) Kotsokechagia, T.; Cellesi, F.; Thomas, A.; Niederberger, M.; Tirelli, N. *Langmuir* **2008**, *24*, 6988.
(20) Rodriguez-Carvajal, J. *Physica B* **1993**, *192*, 55.
(21) Rodriguez-Carvajal, J. *Commis. Powder Diffr. (IUCr) Newslett.* **2001**, *26*, 12.
(22) Howard, C. J.; Sabine, T. M.; Dickson, F. *Acta Crystallogr., Sect. B: Struct. Sci.* **1991**, *47*, 462.
(23) Cerenius, Y.; Ståhl, K.; Svensson, L. A.; Ursby, T.; Oskarsson, Å.; Albertsson, J.; Liljas, A. *J. Synch. Rad.* **2000**, *7*, 203.

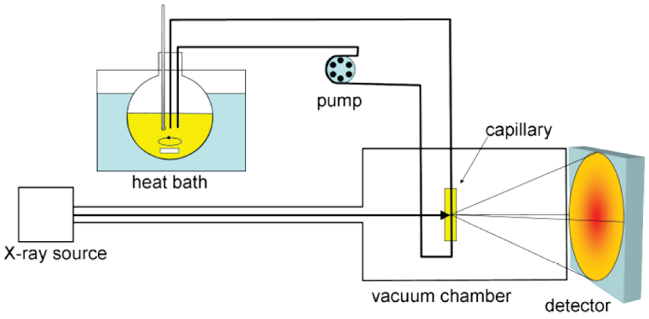

Figure 1. Setup for time-resolved SAXS measurement. The sol is continuously circulated by a peristaltic pump from the solution flask placed in the heat bath through hoses into the quartz capillary placed in the vacuum chamber of the SAXS instrument. The path from the X-ray source to the detector is one integrated vacuum.

detector readout time of 4.3 s, leads to a turnover time of 34.3 s per data frame. The frames were processed using Fit2D[24,25] to yield the integrated powder patterns.

All diffraction patterns were refined by the Rietveld method, using the program GSAS[26] in a batch manner, allowing for automatic refinement of all data. The data were refined from the end of the experiment toward the beginning. The atomic positions and displacement parameters were kept fixed at literature values.[22] The profile model was simpler than that used for the higher-quality ex situ data and allowed only for the refinement of two Lorentzian anisotropic size broadening parameters, with the *c*-axis being the anisotropic broadening axis. The scale factor was refined for all patterns, whereas lattice and size broadening parameters were kept fixed for the first 13 data points, because there essentially is no diffraction information in these first frames.

In Situ SAXS. The SAXS measurements were performed on the modified NanoSTAR instrument at the Department of Chemistry, Aarhus University, using Cu Kα radiation from a rotating anode.[27] The in situ data were collected using a home-built flow-through cell with a circulation setup (see Figure 1). The reaction was performed at 85 °C in a flask in an oil bath next to the sample vacuum chamber. The reaction mixture was continuously pumped through platinum-cured silicone hoses (Masterflex Model 96410-14) into the vacuum chamber, through a 1.7-mm capillary for exposure to the X-rays, out of the vacuum chamber and back into the reaction flask. All hose connections in the circuit were made of either Teflon or Kel-F, because metals were dissolved/etched by the reaction mixture.

The flow rate was 21 mL/min. The hoses held ~5 mL and the reaction mixture had a total volume of 117 mL, including $TiCl_4$, benzyl alcohol, and ethanol (however, the reaction flask was not completely sealed, giving the possibility of some minor (ethanol) evaporation). All hoses were thermally insulated, to reduce heat loss during circulation. The benzyl alcohol was first heated while circulating it through the system. Freshly prepared $TiCl_4$/ethanol solution was added when the temperature was stable at 85 °C, and data collection was started immediately afterwards. In this way, the temperature was held constant from the very beginning of the experiment. The intensity ($I(q)$) was measured for scattering vector lengths (defined as $q = (4\pi \sin\theta)/\lambda$) from 0.00854 $Å^{-1}$ to 0.345 $Å^{-1}$. The first 70 frames were recorded for 5 min each, and the next 120 frames for 1 min each, giving a total measurement time of slightly less than 8 h. The data were not corrected for absorption, because of the relatively low titania concentration, and were normalized to an absolute scale using the SAXS signal of water measured in a different capillary; note that the use of a different capillary in this procedure reduces the precision of the absolute normalization.

The particle formation process can be followed directly from the SAXS data by the invariant Q from the two-phase Porod model:[28]

$$Q = \int_0^\infty I(q)q^2 \, dq = 2\pi^2 \Phi_P (1 - \Phi_P)\overline{(\Delta\rho)^2} \qquad (1)$$

where $\Delta\rho$ is the excess scattering length density of the particles and Φ_P is the volume fraction of particles in the solution. For $\Phi_P \ll 1$, which is valid for the titania particle solution, Q is then proportional to the total volume of particles in the sample. Since $I(q)$ is only measured in a limited q-interval, extrapolation is necessary outside this interval. For measured q higher than 0.2 $Å^{-1}$, a fit was performed to the Porod equation $I(q) = Aq^{-4} + B$, which is the expected power law when surface scattering dominates. The background scattering B was subtracted from all data points while the extrapolation of this fit was applied to perform the integration at high q. At low q, $I(q)$ was extrapolated as being constant and was set equal to the value at the lowest q value of the experiment; note that the low q contribution to the integral is less important, because of the multiplication of $I(q)$ by q^2 in the integrant. For short times, no particle scattering is observed and the extrapolation at high q is not meaningful. However, the estimated Q values are close to zero and, in the plots, the values are displayed as zeros. The measured data, on average, correspond to 75.7% of the total value of Q, with the remainder coming from the extrapolation.

From the invariant (eq 1), it is possible to estimate the particle volume fraction Φ_P, provided suitable estimates for the scattering contrast ($\Delta\rho$) are available. We estimated the scattering contrast using the densities of anatase and benzyl alcohol and could then calculate the particle volume fraction.

After the first period of time with essentially no scattering, the data show scattering from particles. The scattering levels off at low q, which shows the presence of a Guinier regime, in agreement with the particles having a size of

(24) Hammeersley, A. P. FIT2D: An Introduction and Overview, ESRF Internal Report, No. ESRF97HA02T, **1997**.
(25) Hammersley, A. P.; Svensson, S. O.; Hanfland, M.; Fitch, A. N.; Häusermann, D. *High Pressure Res.* **1996**, *14*, 235.
(26) Larson, A. C.; Von Dreele, R. B. *General Structure Analysis System (GSAS)*, Los Alamos National Laboratory Report No. LAUR 86-748, Los Alamos National Laboratory, Los Alamos, NM, 2000.
(27) Pedersen, J. S. *J. Appl. Crystallogr.* **2004**, *37*, 369.
(28) Porod, G. *Kolloid Z.* **1951**, *124*, 83.

a few nanometers. Later in the process, an increase in scattering at low q is observed, which is due to the presence of larger particles or aggregates. In addition, transmission electron microscopy (TEM) shows that the samples consist of aggregates of particles; therefore, the SAXS models were developed to describe this.

The q dependence of the SAXS data was modeled using least-squares fitting of two different models, both of which consist of aggregates of primary particles:[29] (1) polydisperse spherical aggregates of particles and (2) fractal aggregates of particles. In both models, the primary particles were modeled as polydisperse cylinders, in agreement with the crystallite shape determined by PXRD (see below). Attempts to fit the data using polydisperse spheres as primary particles gave fits of lower quality. The model was expressed as $I(q) = AS(q)\langle P(q)\rangle$, where A is a fitted scale factor that takes the contrast, particle volume, and concentration into account, $S(q)$ is the structure factor that describes the position of the primary particles within the aggregates, and $\langle P(q)\rangle$ is the average form factor of the primary particles. The form factor of cylinders is given as[30]

$$P(q) = \int_0^{\pi/2} \left[\frac{2J_1(qr\sin\alpha)}{qr\sin\alpha}\frac{\sin(qL\cos\alpha/2)}{qL\cos\alpha/2}\right]^2 \sin\alpha\, d\alpha \tag{2}$$

where $J_1(x)$ is the first-order Bessel function, r the radius of the cylinder, and L the length. Polydispersity of the cylinders was included, assuming an affine polydispersity and a Schulz distribution[31] of the sizes with a fixed relative width of $\sigma/r = 0.2$. In the numerical integrations, the distribution was truncated at $\langle r\rangle + 10\sigma$, with $\langle r\rangle$ being the average value of r.

The structure factor of model (1) is that of polydisperse spherical aggregates.[32] At low q, the structure factor of an assembly of many particles is described by the form factor of the aggregate. At high q, the scattering intensity must approach that of the constituting particles; therefore, the structure factor must approach unity at high q. With this, we have the following for a monodisperse spherical aggregate:

$$S(q) = 1+(N-1)\left\{\frac{3[\sin(qR)-qR\cos(qR)]}{(qR)^3}\right\}^2 \tag{3}$$

The expression in the curly brackets gives the scattered amplitude from a sphere of radius R, which is then the radius of the aggregate. N is the number of particles within an aggregate. For polydisperse spherical aggregates, the expression becomes

$$S(q) = 1+(N_w-1)\times \frac{\int_0^{\langle R\rangle+10\sigma_R} R^6 f_{Schulz}(R,\langle R\rangle,\sigma_R)\{3[\sin(qR)-qR\cos(qR)]/(qR)^3\}^2\, dR}{\int_0^{\langle R\rangle+10\sigma_R} R^6 f_{Schulz}(R,\langle R\rangle,\sigma_R)\, dR} \tag{4}$$

where N_w is the weight-average number of primary particles within an aggregate. Since the sphere scattering is normalized, N_w is equal to $S(q = 0)$. In this expression, the polydispersity of the aggregates is described by a Schulz distribution $f_{Schulz}(R,\langle R\rangle,\sigma_R)$[31] of the radius R with a width σ_R and truncated at $\langle R\rangle + 10\sigma_R$. The mean-square radius of gyration of the aggregates was calculated by numerical integration over the size distribution

$$\langle R_g{}^2\rangle = \frac{3\int_0^{\langle R\rangle+10\sigma_R} R^8 f_{Schulz}(R,\langle R\rangle,10\sigma_R)\, dR}{5\int_0^{\langle R\rangle+10\sigma_R} R^6 f_{Schulz}(R,\langle R\rangle,10\sigma_R)\, dR} \tag{5}$$

The width of the Schulz distribution obtained by least-squares fitting of the data is uniformly very large: $\sigma_R/R \approx 1$ (1.1(6), on average), meaning that the distribution is essentially exponential.[31]

The structure factor of model (2) is that of a fractal structure. A fractal[33] is a ramified structure with statistical self-similarity in a range of length scales larger than the primary particle characteristic size r_0, and smaller than an upper cutoff length ξ. For fractals, the structure factor follows q^{-D} for $1/\xi \ll q \ll 1/r_0$, where D is the fractal dimension. For usual volume fractals, the value of D lies between unity and 3, where the former can be obtained for linear chain objects and the latter value is approached for compact objects. However, surface fractals can also give rise to power-law scattering and, in this case, effective D values of 3−4 are obtained.[34] In this case, the interpretation is that the scattering follows q^{6-Ds}, where D_s is the surface dimension, the value of which lies between 2 (smooth surface) and 3 (rough surface). In the current work, we will use the model expression by Teixeira[35] for volume fractals for fitting the data and, depending on the value of the (effective) fractal dimension, we interpret it as either originating from a volume fractal ($D = 1-3$) or a surface fractal ($D = 3-4$).

The structure factor for the fractal aggregate is given by

$$S(q) = 1 + \beta\frac{1}{(qr_0)^D}\frac{D\Gamma(D-1)}{[1+1/(q\xi)^2]^{(D-1)/2}}\sin\left[(D-1)\tan^{-1}(q\xi)\right] \tag{6}$$

where r_0 is an equivalent sphere radius of the cylindrical primary particles. β is related to the weight-average number of particles in the aggregate N_w by

$$N_w = S(q=0) = 1+\beta\Gamma(D+1)\left(\frac{\xi}{r_0}\right)^D$$

where the expression for the forward scattering from a fractal (the second term of $S(q = 0)$ without the factor β) is also given by Teixeira. The radius of gyration (R_g) of the volume fractal is given by[35]

$$R_g{}^2 = \frac{D(D+1)\xi^2}{2} \tag{7}$$

(29) Pedersen, J. S. *Adv. Colloid Interface Sci.* **1997**, *70*, 171.
(30) Fournet, G. *Bull. Soc. Fr. Minéral. Crist.* **1951**, *74*, 39.
(31) Kotlarchyk, M.; Stephens, R. B.; Huang, J. S. *J. Phys. Chem.* **1988**, *92*, 1533.
(32) Hansen, S.; Bauer, R.; Lomholt, S. B.; Quist, K. B.; Pedersen, J. S.; Mortensen, K. *Eur. Biophys. J.* **1996**, *24*, 143.
(33) Freltoft, T.; Kjems, J. K.; Sinha, S. K. *Phys. Rev. B* **1985**, *33*, 269.
(34) Bale, H. D.; Schmidt, P. W. *Phys. Rev. Lett.* **1984**, *53*, 596.
(35) Teixeira, J. *J. Appl. Crystallogr.* **1988**, *21*, 781.

At early stages, the SAXS intensity is very low and the models were only fitted to data for $t \geq 112$ min. The data were fitted for $q > 0.01$ Å^{-1} (see Figure 6B).

For the fits to both models, the length of the primary cylindrical particles was fixed. This is because the SAXS curve does not contain information on the length of the particles for aggregated cylindrical prolate particles, since this information is masked by the structure factor of the aggregates. Furthermore, the analysis of the SAXS data shows that the particles, essentially from the moment of formation, are present in the form of small oligomeric aggregates (see Figures 6F−H, presented later in this work). Therefore, the length cannot be fitted and was fixed at an average value of 3 nm for all fits. This value is consistent with the length of the crystals shortly after formation, as observed by in situ PXRD. Test fits with different values of the cylinder length show that only N_w is very sensitive to the choice of cylinder length. Graphs comparing results with cylinder lengths of 3 nm and 6 nm are given in Figure S3 of the Supporting Information. The fact that N_w is influenced by the cylinder length is logical, considering that the amount of inorganic material in the aggregate is constant. A larger cylinder length corresponds to saying that each particle accounts for a larger fraction of the total amount of inorganic material and, consequently, N_w is reduced. In the in situ XRD experiments, the crystallite length, corresponding to the cylinder length, was observed to increase during the experiment. This would result in the true value of N_w increasing less steeply than in the current implementation of the SAXS model. However, the volume of inorganic material in an aggregate, which is given as $V_{MiA} = N_w V_{cyl}$, is not as sensitive to the coupling of N_w as L_{cyl}; hence, we will use V_{MiA} in our further discussions instead.

The number density of aggregates can be calculated from the models and used to estimate the volume fraction of TiO_2. Since the cylinder form factors are normalized so that $P(q = 0) = 1$, and since $S(q = 0) = N_w$, the total scattered intensity at zero angle becomes $I(q = 0) = AN_w$, where A is the fitted scale factor. Using the relation

$$I(q=0) = KMc = \left(\frac{Nm_{aggregate}}{V}\right) KM_{aggregate}$$

$$= \left(\frac{N}{V}\right)\left(\frac{\Delta\rho^2}{\rho_{TiO_2}{}^2}\right) m_{aggregate}{}^2 = \left(\frac{N}{V}\right) \Delta\rho^2 N_w{}^2 V_{cyl}{}^2$$

such that

$$\frac{N}{V} = \frac{I(q=0)}{\Delta\rho^2 N_w{}^2 V_{cyl}{}^2} = \frac{A}{\Delta\rho^2 N_w V_{cyl}{}^2}$$

where K is the scattering constant of the particles and can be given as $K = \Delta\rho^2/(\rho^2 N_A)$, where $\Delta\rho$ is the scattering contrast of the particles (in units of cm^{-2}), ρ their density, and N_A Avogadro's number. M is the molar mass of the scattering particles. Here, we use the molar mass of the aggregate ($M_{aggregate}$). c is the concentration of the scattering particles (given in units of g/cm^3) and is thus given as $c = Nm_{aggregate}/V$, where N is the number of particles in the scattering volume V and $m_{aggregate}$ is the mass of the aggregate. V_{cyl} is the volume of one of the cylindrical primary particles.

We use a contrast calculated for anatase in benzyl alcohol. All other parameters are determined in the model fits. From this expression, the volume fraction of inorganic material (Φ_P) is obtained from the relation $\Phi_P = N_w V_{cyl} N/V$; this term can be directly compared to that obtained from the invariant.

In Situ Turbidimetry. Turbidity measurements were performed on a Perkin−Elmer Model Lambda 25 spectrophotometer. Test spectra suggested that a wavelength of 1000 nm would be suitable for the in situ turbidity measurements. To appreciably scatter light, particles must have a different index of refraction from that of the solvent and sizes on the same order of magnitude as the light wavelength; therefore, the present experiment is mainly sensitive to large assemblies resulting from aggregate formation. The reaction mixture was loaded into a 1-mm-thick quartz cell, to ensure that light was transmitted late in the process. A thermometer that was connected to a Peltier temperature controller was placed at the top of the cell that was touching the reaction mixture, since the cell was too narrow for the thermometer to be fully immersed. This results in a measured temperature that is lower than the actual cell temperature. To ensure that the reaction mixture in the cell had the correct temperature, the sample was heated to the desired temperature before it was transferred to the sample cell, which was also heated in advance in the spectrophotometer heating block. The thermometer showed a temperature of typically 15 °C below the set temperature and decreased no more than ca. 1 °C during the experiment. This was taken as an indication of a constant temperature of the desired value. In a typical experiment, the absorbance was measured every 30 s. In situ turbidity measurements were performed at temperatures of 80, 85, 90, 95, and 100 °C.

Results and Discussion

Ex Situ PXRD. The PXRD patterns all coincide with the expected pattern for the tetragonal anatase. To obtain a good Rietveld fit, it was necessary to include anisotropy of the crystallite shape, which was done by an expansion in surface harmonics. This is clearly seen from Rietveld fits of the 120 °C data with and without anisotropic size broadening, as shown in Figure 2. The resulting shapes were very similar to rectangular boxes elongated along the crystallographic c-axis.

Parameters from the Rietveld refinement are shown in Table 1. The obtained crystal sizes parallel and perpendicular to the crystallographic c-axis are plotted in Figure 3, and they clearly show that the crystals have a prolate shape. The equivalent isotropic crystal size, estimated from an assumed box-shaped crystal as $(size_a{}^2 size_c)^{1/3}$, varies over a range of 2.6−6.0 nm.

For the 80 °C synthesis, the reaction was stopped after 20.50 h. Half of the reaction mixture was left at the synthesis temperature for a total reaction time of 45.75 h.

The results from the Rietveld refinement of these two products indicate that the longer reaction time give slightly larger and significantly more anisotropic crystals. The crystal size increases with reaction temperature, and a similar tendency is observed for the size anisotropy (see Table 1). However, as the reaction times were varied in the present series of syntheses, no quantitative analysis of this behavior has been performed.

In Situ PXRD. Figure 4A shows the background-corrected in situ diffraction data collected at 85 °C. After an induction time, the Bragg peaks start to grow in intensity. All diffraction patterns were refined using the Rietveld method, again including parameters allowing for anisotropic crystal size. For these refinements, only two size parameters were used, respectively, for the size parallel and perpendicular to the crystallographic *c*-axis. This is in accordance with the Rietveld refinement of the ex situ PXRD data that showed that the particles are almost box-shaped. Figure 4B shows the scale factor extracted from the refinements. After an induction time of ~60 min, crystals form and the scale factor then rises until ~190 min. Thereafter, it levels off and starts to decrease, the latter being a result of sedimentation of particles out of the beam. The entire dataset, as a function of time t, could be fitted with a simple sigmoidal growth model with a linear sedimentation loss that begins after a given time t_s:

$$S(t) = S_\infty(\{1 - [1 + \exp(\frac{t - t_r}{d_t})]^{-1}\} - s_s(t - t_s))$$

where S_∞ is the intensity at infinite time, t_r the inflection time, and d_t the characteristic growth time. The latter linear term represents the decrease in intensity that is due to sedimentation and t_s is the sedimentation onset time; s_s is the sedimentation rate. The term s_s is only refined for $t > t_s$ and is zero otherwise. This simple model fits the entire dataset (with a correlation coefficient of fit of R^2 = 0.99811) and yields the following values: t_r = 141.9(3) min, d_t = 24.3(2) min, t_s = 220.0(3) min, and s_s = 0.0204(5) min^{-1}. The scale factor plot suggests that crystal growth and sedimentation are decoupled in the sense that sedimentation seems to set in after the rapid growth phase is over.

The Rietveld refinement allowed refining of lattice constants and crystallite sizes only for times greater than

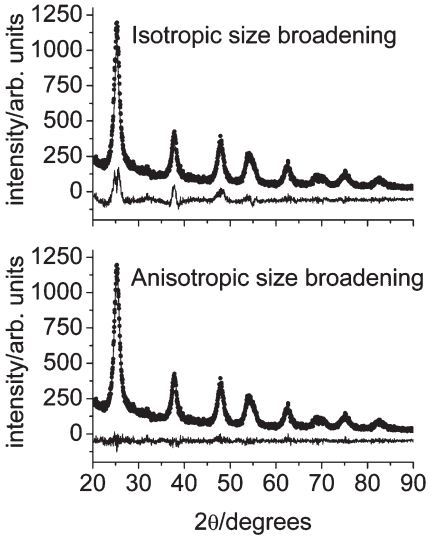

Figure 2. Rietveld refinement of PXRD data from the product of the synthesis at 120 °C with Rietveld fits for both isotropic (top) and anisotropic (bottom) crystallite size models. The observed data are shown as dots, while the model is drawn as a solid line. The difference between observations and model are given as a full line offset by −50 along the coordinate axis.

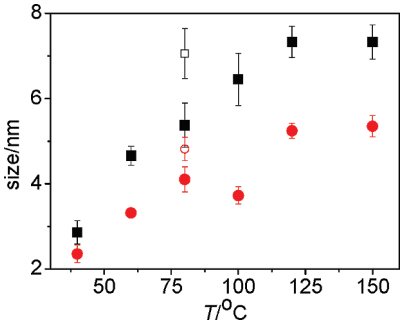

Figure 3. Crystallite size parallel (solid black squares) and perpendicular (solid red circles) to the *c*-axis from peak broadening of ex situ PXRD patterns for anatase nanoparticles synthesized at temperatures in the range of 40−150 °C. (Note that the reaction time is not constant.) Empty symbols represent data for product left at 80 °C for further reaction (from 20.50 h to 45.75 h). When error bars are not visible, the standard uncertainty is smaller than the symbol. Note that the standard uncertainty shown is that obtained from least-squares refinement and, therefore, is only a measure of the relative precision of the determination of the given number.

Table 1. Results from Rietveld refinement of Ex Situ Powder Diffraction Data Using an Anisotropic Particle Size and Shape Description Based on Linear Combinations of Spherical Harmonics

synthesis temperature, T (°C)	duration of synthesis, t (h)	Fit Quality Parameters		Lattice Constants of the Tetragonal Anatase Lattice		Effective Crystal Size (nm)[a]		size anisotropy (%)[b]
		χ^2	Rp	a (Å)	c (Å)	size$_a$	size$_c$	
40	504	1.052	15.0	3.8034(19)	9.454(4)	2.4	2.9	17
60	120	1.094	14.7	3.7947(7)	9.5017(19)	3.3	4.7	30
80	20.5	1.058	21.5	3.7979(12)	9.511(3)	4.1	5.4	24
80	45.75	1.049	20.7	3.7960(9)	9.5167(24)	4.8	7.1	32
100	4	1.133	16.6	3.7980(11)	9.510(3)	3.7	6.5	43
120	1.33	1.139	13.7	3.7921(6)	9.5163(15)	5.2	7.3	29
150	0.25	1.232	23.7	3.7936(8)	9.5030(20)	5.4	7.3	26

[a] The term size$_a$ refers to the effective crystal size perpendicular to the crystallographic *c*-axis, whereas the term size$_c$ refers to the effective crystal size parallel to the crystallographic *c*-axis. [b] Size anisotropy is defined as (size$_c$ − size$_a$)/size$_c$, expressed as a percentage.

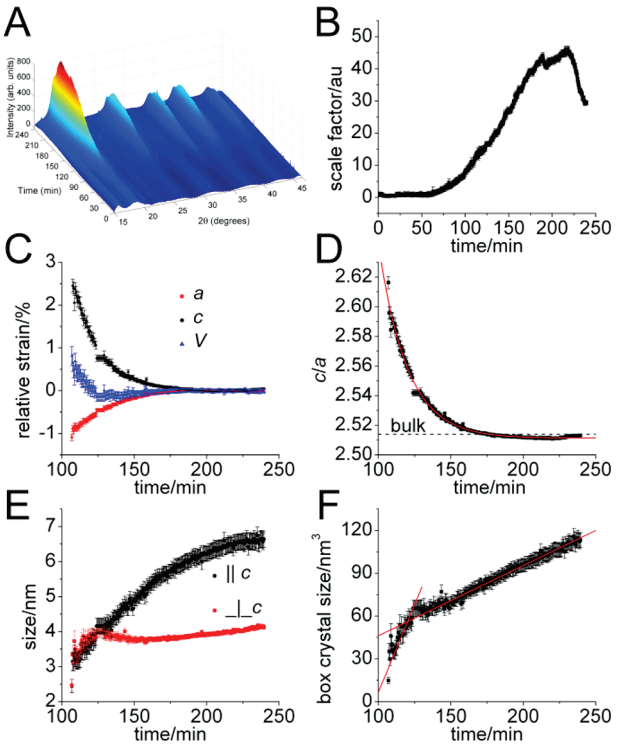

Figure 4. Results from in situ PXRD: (A) background-subtracted raw data; (B) scale factor from Rietveld refinement; (C) relative strain calculated from the refined lattice parameters, with respect to the lattice parameters at the end of the experiment (see text); (D) ratio of the tetragonal lattice constants c and a, as a function of time (the dashed line indicates the expected value for bulk anatase; the red line is a fit to an exponential decay); (E) crystal size parallel (black) and perpendicular (red) to the crystallographic c-axis; and (F) simplified total crystal size, assuming a box crystal shape and using the sizes shown in panel (E) (the red lines are linear fits).

106.9 min, because the intensity of the Bragg signals was too close to the background for shorter times. Figure 4C presents the time evolution of the lattice constants, shown as relative strain calculated by $s_a(t)\,(\%) = 100 \times (a - a_\infty)/a_\infty$, where a_∞ is calculated from the average lattice constants in the time window of 214.9−226 min (later data are excluded, because of a small effect on the lattice constants from the sedimentation process); similar equations apply for the c-axis and the unit-cell volume. At shorter times, there is a very large positive relative strain (expansion) of the c-axis (2%−2.5%), while the a-axis is compressed up to 1%. The relative strains on a and c relax in an exponential fashion with decay times of 23.6(5) and 18.2(3) min for the a- and c-axes, respectively. The unit-cell volume shows a much smaller effect, because the relative strains on a and c almost cancel, so that the volume relative strain starts positive with a downward slope, reaches a minimum on the compressive side, and gradually relaxes thereafter to zero relative strain. The c/a ratio also deviates strongly (up to 4%) from the bulk value, as a result of the different relative strain in the a- and c-directions. The time evolution of the c/a ratio is shown in Figure 4D, which shows an exponential relaxation of the deviation from the bulk value with a decay time of 19.63(23) min. The observation of positive transient relative strains during growth is surprising since ex situ measurements of the size dependence of lattice relative strain for round particles consistently show a negative relative strain for both axes, with the c-axis displaying the largest relative strain.[36] Our ex situ measurements (see Table 1) also display this behavior. We will return to this point later in the discussion.

The time evolution of the size of the nanocrystals is shown in Figure 4E. Interestingly, the crystallites are initially almost spherical and crystallite shape anisotropy does not begin until after a period of spherical growth of ∼155 min. Growth continues along the c-axis, while it essentially stops along the a-axis and only later appears to pick up again at a much slower pace. There is even an indication that the size along the a-axis may shrink, corresponding to selective particle dissolution in this direction, just after the onset of anisotropic growth. The entire growth sequence along the c-axis can be fitted to a single Boltzmann growth model:

$$\mathrm{size}_{||c}(t) = \mathrm{size}_{||c,\infty}\{1 - [1 + \exp(\frac{t - t_{g||c}}{d_{g||c}})]^{-1}\}$$

where $\mathrm{size}_{||c,\infty}$ is the size along the c-direction at infinite time, $t_{g||c}$ the onset time, and $d_{g||c}$ the characteristic growth time. With this expression, the fit quality is $R^2 = 0.99267$ and $\mathrm{size}_{||c,\infty} = 6.89(6)$ nm, $t_{g||c} = 115.3(8)$ min, and $d_{g||c} = 37.4(1.4)$ min. The much more complicated situation along the a-axis has not been modeled. An estimate of the total crystallite size can be made by assuming a box-shaped crystal from $V_{\mathrm{box\ crystal}} = \mathrm{size}_{||a}{}^2\mathrm{size}_{||c}$, where $\mathrm{size}_{||a}$ is the crystallite size perpendicular to the c-axis. This estimated crystallite volume is shown in Figure 4F. Most interestingly, the box volume growth seems to be much simpler: an effectively linear growth with different slope before and after the transition to anisotropic particle growth. The linear growth rates are on the order of 3.1 and 0.5 nm^3/min before and after the transition to anisotropic growth, respectively. This apparent linearity is obviously an oversimplification, but the rates derived from there still illustrate the much more rapid overall growth rate in the isotropic growth region.

Plotting the absolute strain based on the room-temperature lattice constants of Howard et al.,[22] as a function of particle size (see Figure S5 in the Supporting Information) shows a crossover from positive to negative strain for the c-axis at an equivalent linear particle size of 4.0(1) nm (or for a length of the crystal along the c-axis of 4.2(2) nm). This suggests that the observed positive strain along the c-axis is related to the onset of shape anisotropy. This is seen in Figure 5A, which shows the observed lattice strain versus the particle size anisotropy, as a percentage, calculated as $[(\mathrm{size}_{||c}/\mathrm{size}_{\perp c}) - 1] \times 100$. The crossover to negative strain along the c-axis occurs at the onset of a positive particle size anisotropy (corresponding to a transition to prolate particles). The strains then gradually saturate at the final negative values as the size anisotropy

(36) Zhang, H.; Chen, B.; Banfield, J. F. *Phys. Chem. Chem. Phys.* **2009**, *11*, 2553.

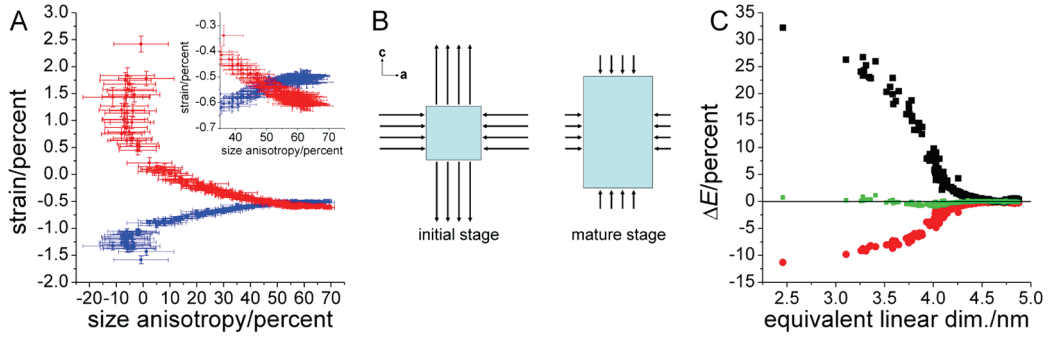

Figure 5. Lattice strain versus particle shape anisotropy: (A) absolute lattice strain (see text) of the *a*- axis (blue symbols) and the *c*-axis (red symbols), determined from in situ powder diffraction plotted against crystal size anisotropy ($(\text{size}_{\parallel c}/\text{size}_{\perp c} - 1) \times 100\%$) (the inset shows an enlargement of the large shape anisotropy values for which the strain saturates); (B) sketch of particles with the dimensions reflecting those found by in situ PXRD (light blue boxes) and effective strain (arrows) of crystals in the initial stage of growth (left) and in the mature stage (corresponding to 60% size anisotropy, right) (the length of the arrows gives relative strain magnitude, whereas the orientation gives the direction (arrows pointing away (toward) denoting positive (negative) strain)); and (C) Ti−O bond energy variations resulting from the strain (see text) (each Ti atom has two bonds parallel to the *c*-axis (black squares) and four roughly in the *a*,*b*-plane (red circles); the total relative Ti bond energy is shown in green symbols).

increases and are effectively constant at a size anisotropy above ~55%; this behavior is sketched in Figure 5B, which shows schematic drawings of initial and late stage crystals and the accompanying strain. The effect of thermal expansion does not alter this effect, as found by using lattice constants derived from the thermal expansion study of Hummer et al.[37] (not shown).

The observed anisotropic strain can be related to the surface stress, pressure, and energy. The total surface energy (i.e., the free energy needed to create a unit area of the surface) of a nanoparticle contains two contributions: an in-plane energy, resulting from the in-plane surface stress, and a "chemical" part, reflecting the presence of different bonding situations (dangling bonds or solvent termination) at the surface.[38,39] The chemical term can be thought of as an out-of-plane contribution. Hence, the surface energy is, in the notation of Ouyang et al.,[38,39] $\gamma = \gamma^{\text{struct}} + \gamma^{\text{chem}}$. Zhang et al. recently investigated the size dependence of the surface free energy based only on the in-plane surface stress (γ^{struct}) of spheroidal anatase nanocrystals synthesized by annealing amorphous precursors.[36] Assuming isotropic particle shape, they calculated the surface stress from the relation

$$f = -\left(\frac{V - V_0}{4V_0}\right)Bd$$

where V is the actual unit cell volume, V_0 the bulk unit-cell volume (such that $(V - V_0)/V_0$ is the volume strain), d the particle diameter, and B the (size-dependent) bulk modulus.[36,40−42] The surface stress is, in turn, related to the surface free energy γ^{struct} (for an isotropic solid) by the expression

$$f = \gamma^{\text{struct}} + A\left(\frac{\partial \gamma^{\text{struct}}}{\partial A}\right)$$

with A being the surface area[36,40,41] so that γ^{struct} can be calculated from f via integration, as done by Zhang et al.[36] The implicit assumption in Zhang et al.'s approach is that the strain originates exclusively from the in-plane structural component, which is a reasonable assumption in their case where the particles were obtained from amorphous precursors. In the spheroidal nanoparticles studied by Zhang et al., the strain predominantly originates from strain along the *c*-axis, even though both the *a*- and *c*-axis strains are negative and range from −0.7% to 0.0% for the *a*-axis and from −0.28% to −0.01% for the *c*-axis. As is evident from the equations above, f (and, consequently, γ^{struct}) is only positive if the strain indeed is negative. In the present case, the surface is ligand-terminated and it can be expected that this strongly influences the strain of these very small particles. Hence, we suggest that the observed large strain is a direct consequence of the surface-bound ligands and that these provide the driving force for anisotropic growth.

The energy difference between the strained and relaxed state can be grossly estimated from the change in the Ti−O bond energy. Each Ti has two long out-of-plane bonds parallel to the *c*-axis and four shorter bonds roughly in the *a*,*b*-plane. Hence, the total bond energy of a single Ti can be estimated from the sum of these contributions. To this end, we use the Matsui−Akaogi potential[43] that has been used in the literature to perform molecular dynamics (MD) simulations of titania polymorphs and nanoparticles.[43−45] The potential between atoms i and j is written as

$$V_{ij} = q_i q_j r_{ij}^{-1} - C_{ij} r_{ij}^{-6} + f B_{ij} \exp\left(\frac{A_{ij} - r_{ij}}{B_{ij}}\right)$$

where r_{ij} is the interatomic distance and $q_{\text{Ti}} = 2.196$ e, $q_{\text{O}} = -1.098$ e, $C_{\text{TiO}} = 1215$ Å^6 kJ mol^{-1}, $A_{\text{TiO}} = 2.8162$ Å, $B_{\text{TiO}} = 0.194$ Å, and $f = 4.184$ kJ Å^{-1} mol^{-1}.[43] For the

(37) Hummer, D. R.; Heaney, P. J.; Post, J. E. *Powder Diffr.* **2007**, *22*, 352.
(38) Ouyang, G.; Tan, X.; Yang, G. *Phys. Rev. B* **2006**, *74*, 195408.
(39) Ouyang, G.; Wang, C. X.; Yang, G. W. *Chem. Rev.* **2009**, *109*, 4221.
(40) Cammarata, R. C.; Sieradzki, K. *Annu. Rev. Mater. Sci.* **1994**, *24*, 215.
(41) Shuttleworth, R. *Proc. Phys. Soc. A* **1950**, *63*, 444.
(42) Chen, B.; Zhang, H.; Dunphy-Guzman, K. A.; Spagnoli, D.; Kruger, M. B.; Muthu, D. V. S.; Kunz, M.; Fakra, S.; Hu, J. Z.; Guo, Q. Z.; Banfield, J. F. *Phys. Rev. B* **2009**, *79*, 125406.
(43) Matsui, M.; Akaogi, M. *Mol. Simul.* **1991**, *6*, 239.
(44) Koparde, V. N.; Cummings, P. T. *J. Phys. Chem. B* **2005**, *109*, 24280.
(45) Swamy, V.; Gale, J. D.; Dubrovinsky, L. S. *J. Phys. Chem. Solids* **2001**, *62*, 887.

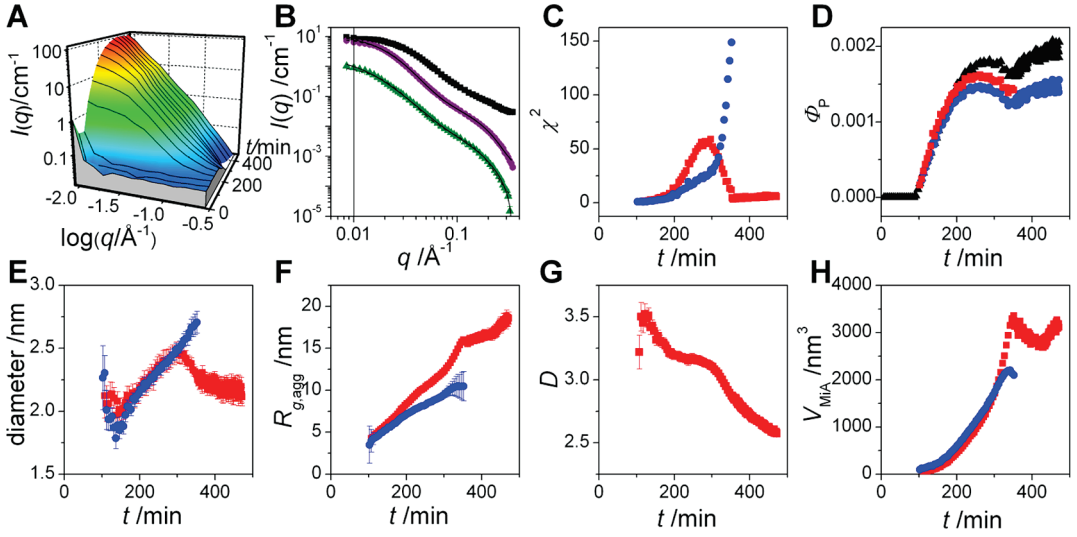

Figure 6. Results from in situ SAXS. (A) Surface plot of the time-resolved data. (B) Figure showing selected data and corresponding fits, where the data have been fitted by two models (spherical and fractal aggregates; see text for details). The data are for t = 152 min (black symbols, top), t = 277 min (purple symbols, middle), and t = 400 min (green symbols, bottom). The fits to the two modes are shown as full and dotted lines for the fractal and spherical models, respectively. Data are presented on an absolute scale for t = 152 min, while the plots for t = 277 and 400 min have been divided by 10 and 100, respectively, for the sake of clarity. Fit parameters are shown in blue for the spherical model and red for the fractal model. (C) Reduced χ^2 for fits of the two models. (D) Particle volume fraction (Φ_P) calculated from the invariant (black symbols represent data from the text, blue symbols represent data from the spherical model, and red symbols represent data from the fractal model). (E) Diameter of cylindrical primary particles (length of 3 nm). (F) Radius of gyration of aggregates in the two models. (G) Fractal dimension of the fractal aggregate. (H) Volume of inorganic material bound in an aggregate (see text).

small highly strained particles, the Ti−O bond parallel to the *c*-axis is highly weakened. Relative to the bond energy for the mature particles (the time regime used to calculate the relative strain in Figure 4C), the bond is weakened by up to 32% (see Figure 5C). However, the shortened bonds in the *a,b*-plane have a higher relative bond energy and are up to 11% stronger. However, the total Ti bond varies much less and the total bond energy is maximally 1% less stable in the initial nanocrystals, compared to the relaxed state, and varies only slightly with the particle size (it should be stressed that these estimates ignore the O···O and Ti···Ti (and longer-range) interactions that also vary). This strongly supports the view that the structural distortion is the result of ligand binding to the surfaces. The benzyl alcohol has been suggested to preferentially attach to the {101} faces of anatase, leading to the anisotropic particle shape.[46] In the present case, ethanol was used to presolvatize the $TiCl_4$, and this may have influenced the surface coverage.[19] Nevertheless, anisotropic ligand binding would certainly account for the distortion of the Ti binding environment, leading to the large anisotropic strain and providing the impetus for anisotropic growth.

In Situ SAXS. The SAXS data are shown in Figure 6A. Selected spectra that are shown in Figure 6B illustrate how the SAXS patterns evolve with time. Information on particle formation is obtained directly from the data by calculation of the invariant Q, which is simply related to the particle volume fraction (see Experimental Section); the thus-extracted particle volume fraction (Φ_P) is plotted as a function of time t in Figure 6D. It is initially zero (also see the Experimental Section) and increases from zero at t = 92 min, as a result of particle formation. After a period of rapid growth, the increase in Φ_P slows. The decrease after 300 min can be explained by scattering outside the available q-range (to the low q side) from larger particles/aggregates. The onset of particle formation at t = 92 min corresponds very well with the time of crystal formation observed from the in situ PXRD experiment (Figure 4), indicating that crystalline particles are present from the moment of particle formation. The final particle volume fraction calculated from the invariant is ~0.002. The number concentration of aggregates was calculated as described in the Experimental Section and is shown in Figure S4 of the Supporting Information. As expected, the number concentration of aggregates increases at first but then decreases as the particles aggregate into larger and larger aggregates; the final aggregate concentration is ~0.8 μM (see Figure S4 in the Supporting Information).

Full conversion to TiO_2 (100% yield) would result in a mass fraction of Φ^m_{Full} = 0.0181 (see the Supporting Information). The measurement of isolated dry solid after 24 h of reaction gave a TiO_2 yield of 89.0%, corresponding to a mass fraction of Φ^m = 0.0161. The invariant estimate corresponds to a value of Φ^m = 0.00785 (~43%), assuming that the inorganic part of the particles has the density of anatase. The discrepancy between the two estimates, by a factor of ~2, can be attributed to the difficulties in absolute calibration of the SAXS data, the fact that no absorption correction was applied, scattering outside the probed q-range from larger aggregates (see above) (which would lead to an estimate of the volume fraction that was too low), and from possible additional anatase precipitation during the centrifugation step used in isolation of the solid. In view of these sources of error, we find that the agreement is satisfactory.

(46) Polleux, J.; Pinna, N.; Antonietti, M.; Hess, C.; Wild, U.; Schlögl, R.; Niederberger, M. *Chem.—Eur. J.* **2005**, *11*, 3541.

The SAXS data were fitted with two models, which involve cylindrical primary particles that form (1) spherical aggregates or (2) fractal aggregates, as discussed in detail in the Experimental Section. The fit quality, represented by the reduced χ^2 of the least-squares fitting, is shown in Figure 6C and can be determined from the example curves in Figure 6B. Before $t = 112$ min, essentially no particle scattering is observed, which again fits nicely with the time of crystal formation from the PXRD results. The models are then only fitted to the data from this time. Up to 200 min, the fractal model and the spherical model fit the data equally well. Thereafter, there is a period of time where both models fit the data less well, but after ~300 min, the sphere model no longer fits the data and the fractal model fits the data increasingly well. This suggests that there is a crossover in aggregation behavior during the growth process. Results for the spherical aggregate model are not shown for later times, because of its poor agreement with the data. The cylinder diameters for the two models are plotted in Figure 6E. They are calculated as scattering weighted values, i.e., as the square root of the ratio of eighth and sixth moments of the size distribution (see eq 5), to make them directly comparable to the crystallite size obtained from PXRD peak broadening. The diameter has a value of ~2.4 nm just after particle formation. After this point, it continues to increase slowly. For the fractal model, it stabilizes at ~2.5 nm after a broad maximum with the maximum size obtained at $t = 277$ min. However, at this time, the fractal model does not fit the data perfectly at high q, where the intensity pattern stems from the primary particles (see Figure 6B). This indicates that one should not rely upon the high values for the diameter as representing the actual particle size. At $t = 400$ min, the fit at high q has improved, and the fit value for the particle size is more credible here.

As an attempt to obtain good fits of the fractal model at all times, we also made fits of an alternative fractal model where the last term on the right-hand side of eq 6 for the fractals was replaced by the empirical expression given by Beaucage.[47] This gave better fits to the data at the intermediate region and more-constant values for the cylinder diameter. However, the results are not shown, because the model has more fit parameters than the fractal model of Teixeira, and, moreover, we still observe a time region of less-good fits.

The radius of gyration of the aggregates for the two models (which is defined as $R_{g,agg} = \langle R_g^2 \rangle^{1/2}$) is plotted in Figure 6F for each of the two models. Just after particle formation, the value of $R_{g,agg}$ is < 5 nm (only twice the cylinder diameter) for both models, indicating that the particles are only slightly aggregated; for the number-averaged sizes, the cylinder and aggregate sizes will be even similar to each other. $R_{g,agg}$ increases until $t = 200$ min (more for the fractal model than for the spherical model), but is still comparable to a few cylinder diameters. Because of the very limited size of the fractal, it is not a true volume fractal, but rather a surface fractal, which is more comparable to a sphere. This is confirmed by the apparent fractal dimension D, which, for these times, has a value of >3(Figure 6G). After $t = 200$, the $R_{g,agg}$ value for the sphere model is considerably smaller than that for the fractal model. However, the volume of inorganic material in an aggregate (Figure 6H) is the same for the two models, meaning that the spherical model describes much denser aggregates than the fractal model. The spherical model fits the data better at these times, indicating that the aggregates are best described by this model. The fractal dimension D remains above 3 until $t = 322$ min, where a crossover to a volume fractal is observed. Here, the χ^2 value for the spherical model (see Figure 6D) is strongly increasing, whereas the fit for the fractal model is improving. It is also at this time that the R_g value of the fractal increases more steeply to a value of 16 nm. Overall, the fit results indicate a transition from a small and compact structure to a ramified fractal structure of larger size. At $t = 353$ min, the fractal model gives a perfect fit to the data.

The particle volume fraction was also calculated from the models and is compared to the values derived from the invariant in Figure 6D. Up to ~200 min, the three estimates agree completely. Thereafter, the model estimates are slightly below that derived from the invariant. Considering the assumptions made regarding the scattering contrast, the density of inorganic material, and the calculation of the invariant, we find that the agreement is satisfactory.

The volume of inorganic material in an aggregate is displayed in Figure 6H. It increases drastically from $t = 100$ min to $t = 300$ min, reaching a volume of ~3000 nm^3. Thereafter, it levels off for the same reasons discussed for the volume fraction in Figure 6D.

In Situ Turbidimetry. Time-resolved turbidity data for reactions performed at temperatures from 80 °C to 100 °C are shown in Figure 7A. The turbidity increases drastically after a lag time that is dependent on the synthesis temperature. Since turbidity is sensitive to particles of

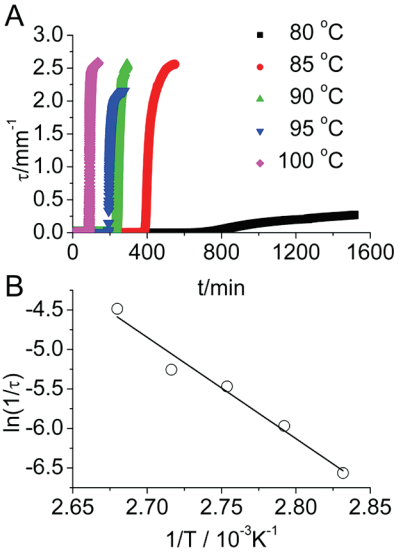

Figure 7. Results from in situ turbidimetry measured at $\lambda = 1000$ nm: (A) turbidity for reactions performed at 80, 85, 90, 95, and 100 °C; (B) Arrhenius plot of time ($1/\tau_i$) versus the increase in turbidity.

(47) Beaucage, G. *J. Appl. Crystallogr.* **1995**, *28*, 717.

several hundred nanometers in size, this is a sign of large-scale particle aggregation. For 85 °C, which is the temperature for the in situ SAXS and PXRD experiments, the increase in turbidity begins at $t_{onset} = 375$ min. This is 25 min after the time where the fractal model starts to fit the SAXS data perfectly (at 350 min; see Figure 6D). This indicates that the fractal aggregates that have been observed via SAXS grow to larger sizes, which are outside the size region probed by SAXS.

The times τ_i for the increase in turbidity were taken to be the intersection with the time axis of a straight line fitted to the steepest part of the increase. For $T = 85$ °C, the τ_i value is 391 min. Calculating the activation energy from an Arrhenius plot of the τ_i values (Figure 7B) gives a value of 106.7(9.8) kJ/mol.

Comparative Analysis of PXRD, SAXS, and Turbidity. For the titania synthesis performed at 85 °C, both the PXRD scale factor and the SAXS invariant increase sigmoidally, with a characteristic time of ~150 min, but over a broad time interval with an onset before 100 min, earliest for the PXRD scale factor. The SAXS modeling results show that ~3-nm cylindrical particles are formed after 112 min. This time corresponds nicely to the time of crystal formation ($t_{g\|c} = 115.3(8)$ min, $d_{g\|c} = 37.4(1.4)$ min). This means that crystalline material is present from the moment of particle formation. Comparing the size of the particles obtained from PXRD and SAXS, respectively, it is apparent that the crystal dimension parallel to the crystallographic *a*-axis (Figure 4E) is larger than the cylinder radius obtained by SAXS (see Figure 5E). This might be caused by the presence of smaller noncrystalline particles or clusters, which are probed by SAXS but not by PXRD.

The SAXS results reveal a transition from a small dense aggregate structure to a larger and more ramified structure at $t \approx 322$ min, where the fractal dimension D drops below a value of 3 (transition from surface to volume fractal). Here, the model of dense spherical aggregates no longer fits the experimental data, whereas the fractal model provides relatively good fits. After $t = 353$ min, the fractal model gives perfect fits to the data. The turbidity measurements show large-scale aggregation at $t = 375$ min, where the turbidity increases drastically. This time is ~50 min after the time of volume fractal formation that was derived from the SAXS data. This supports the interpretation that the appearance of volume fractals indicates large aggregates, and that they grow to give a highly turbid solution at a later time. The size of the final aggregates is not probed by SAXS, because of the limited q range available at low q. This means that both the invariant, giving the total volume of particles in solution, and the radius of gyration of the large aggregates only represent the length scales probed in the experiment and that they are not giving the actual size and amount of the aggregates.

The activation barrier for aggregation might be due to the benzyl groups, which are believed to be attached to the crystallites stabilizing the suspension, thus reducing the tendency to aggregate. By quenching the solution before the large-scale aggregation, it might not be totally prevented, but at least it is slowed drastically to form a metastable dispersion of individual nanoparticles for further solution processing.

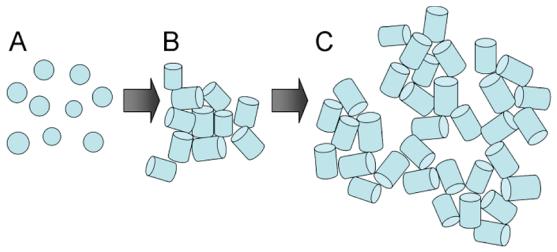

Figure 8. Sketch of the growth process: (A) initially isolated isotropic crystalline nanoparticles are formed (after ~125 min at 85 °C); (B) then, crystal shape anisotropy begins, because of anisotropic ligand binding (~200 min; see text) and the particles form small, dense aggregates; and, finally, (C) the particles growth further and assemble into larger ramified fractal structures (~400 min) that scatter light, resulting in a turbid solution.

Conclusions

The combination of in situ powder X-ray diffraction (PXRD), small-angle X-ray scattering (SAXS), and turbidimetry has allowed for probing of the kinetics of particle formation, crystallization, and aggregation. The combined information obtained from these experiments is sketched in Figure 8. Nanoparticles form with a sudden onset (SAXS) and are, within the time resolution of the experiments, crystalline from their formation (PXRD). This is contrary to what is often observed for sol−gel syntheses.[48−51] The nanocrystals are initially dispersed and spherical in shape (see Figure 8A), but with a very large anisotropic lattice strain that we attribute to differential binding of the coordinating solvents used in the present nonaqueous synthesis. This provides an impetus for anisotropic growth that is much stronger than when, e.g., making anatase via the thermal annealing of preformed amorphous titania.[36,48] These unique insights into the coupled evolution of lattice strain and particle size and shape underline the importance of in situ diffraction studies for understanding the mechanisms behind nanocrystal size and shape, which is of key importance for the performance of the ensuing material.

The in situ SAXS data show that the nanocrystals start to aggregate first into small dense clusters of the now anisotropically shaped particles (see Figure 8B). Later, as crystal growth continues to render the crystals more anisotropic in shape, the aggregates change character to larger ramified fractal structures (see Figure 8C), which leads to a sharp onset in turbidity that increases as the aggregates continue to grow and increase in number. The turbidity measurements show that the aggregation is an activated process. Hence, the use of three in situ techniques allowed us to cover the relevant structural length

(48) Zhang, H.; Finnegan, M.; Banfield, J. F. *Nano Lett.* **2001**, *1*, 81.
(49) Wang, C.-C.; Ying, J. Y. *Chem. Mater.* **1999**, *11*, 3113.
(50) Yanagisawa, K.; Owenstone, J. *J. Phys. Chem. B* **1999**, *103*, 7781.
(51) Yang, J.; Mei, S.; Ferreira, J. M. F. *J. Am. Ceram. Soc.* **2000**, *83*, 1361.

scales: Ångström to several nanometers (PXRD), from a few nanometers to hundreds of nanometers (SAXS), and into the micrometer length scale (turbidity). The understanding of the system, summarized in Figure 8, also provides information that will allow, for example, the preparation of small aggregates of nanoparticles (see Figure 8B) by quenching the system in the desired arrested state. Such particles can be further modified in subsequent liquid-phase processing.

Acknowledgment. We thank Dr. Yngve Cerenius for his kind assistance with the in situ synchrotron measurements and DanScatt for funding of the synchrotron parts of this project. We thank Ms. Bente Olsen for her kind assistance with the turbidity measurements, the workshop at the Department of Chemistry, Aarhus University (Mr. Erik Pedersen, Mr. Palle Christensen, and Mr. Eigil Hald) for aid in constructing the in situ apparatuses for SAXS and synchrotron PXRD, and Mr. Jacques Chevallier for helping with the TEM analysis. H.B. thanks the Danish Natural Science Research Council for support through a Skou Associate Professor Fellowship. Additional funding was provided by a grant from the Danish Natural Science Research Council (J.S.P.).

Supporting Information Available: Detailed yield calculation, TGA/DSC analysis of isolated powder, XRD before and after TGA; graphs illustrating the influence of the choice of cylinder length on model parameters in the SAXS fractal model as well as the concentration of aggregates calculated from the two SAXS models; plots of absolute strain as a function of crystallite size parameters. (PDF) This information is available free of charge via the Internet at http://pubs.acs.org.